

Reduced atomic models for large-scale computations: Fe XIII near-infrared lines

Giulio Del Zanna^{1,2*}, Supriya Hebbur Dayananda^{3,4}

¹ DAMTP, Centre for Mathematical Sciences, University of Cambridge, Wilberforce Road, Cambridge CB3 0WA, UK

² School of Physics & Astronomy, University of Leicester, Leicester LE1 7RH, UK

³ Instituto de Astrofísica de Canarias, E-38205, La Laguna, Tenerife, Spain

⁴ Departamento de Astrofísica, Facultad de Física, Universidad de La Laguna, Tenerife, Spain

Submitted to MNRAS

ABSTRACT

Accurate atomic models for astrophysical plasma can be very complex, requiring thousands of states. However, for a variety of applications such as large-scale forward models of the Stokes parameters of a spectral line in the solar corona, it is necessary to build much reduced atomic models. We present two examples of such models, focused on the two near-infrared Fe XIII lines observed on the ground at 10750, 10801 Å. These lines are primary diagnostics for a range of missions (especially the Daniel K. Inouye Solar Telescope, DKIST) to measure electron densities and magnetic fields in the solar corona. We calculate the Stokes parameters for a range of coronal conditions using CHIANTI (for intensities) and P-CORONA (for intensities and polarization), and use P-CORONA and a realistic global MHD simulation to show that the reduced models provide accurate results, typically to within 5% those obtained with larger models. Reduced models provide a significant decrease (over three orders of magnitude) in the computational time in spectropolarimetric calculations. The methods we describe are general and can be applied to a range of conditions and other ions.

Key words: atomic data – atomic processes – Solar magnetic fields – Solar coronal lines

1 INTRODUCTION

Accurate atomic models for astrophysical plasma can be very complex, depending on the local environment and which physical processes need to be included. Typically, a large-scale collisional-radiative model needs to be built, to take into account ionization and recombination via Rydberg states, requiring thousands of states (e.g. the helium models by Del Zanna et al. 2020; Del Zanna & Storey 2022).

On the other hand, computationally intensive calculations are becoming necessary. For example, to assess the reliability of three-dimensional (3D) MHD models of the extended solar corona such as those produced by “Predictive Science Inc.” (PSI¹) and compare them to observables (see, e.g. Schad et al. 2023) one needs to calculate the local emissivity over a large volume, and then perform integrations along the line-of-sight (ALOS). A lot more challenging are 3D spectropolarimetric calculations, discussed below. Another obvious example is radiative-transfer calculations in 3D. In all such cases, it is necessary to build much reduced atomic models, but making sure that the results of the computations are ‘close’ to those obtained with the full model. How close depends on a number of factors. First of all on the accuracy of the observables. Secondly,

on the accuracy of the large-scale atomic models, an issue briefly discussed below.

We focus this paper on modelling the Fe XIII lines at 10750, 10801 Å (vacuum wavelengths) first discovered by Bernard Lyot in the 1930s (cf. Lyot 1939), as they are the strongest lines in the near infrared (NIR). There is a growing interest in spectroscopic observations of the solar coronal forbidden lines in the NIR, as they offer powerful diagnostics to measure ionization temperatures, electron densities and chemical abundances, as reviewed in Del Zanna & DeLuca (2018), and to obtain information on the coronal magnetic field with spectropolarimetry (SP), as described e.g. in Judge (1998), Judge et al. (2013), and Penn (2014).

Regular observations of the Fe XIII NIR lines have been carried out with the Coronal Multichannel Polarimeter (CoMP) instrument, described by Tomczyk et al. (2008), and, together with more lines with its upgraded version UCoMP. They are also a target for the Coronal Solar Magnetism Observatory (COSMO), see e.g. Tomczyk et al. (2016); Landi et al. (2016).

The airborne infrared spectrometer (AIR-Spec) has surveyed the NIR during the 2017 and 2019 eclipses (cf. Madsen et al. 2019; Samra et al. 2021; Samra et al. 2022; Del Zanna et al. 2023) as a pathfinder for future observations with the Daniel K. Inouye Solar Telescope (DKIST, see Rimmele et al. 2015) CryoNIRSP spectropolarimeter (Fehlmann et al. 2016). CryoNIRSP is now regularly observing several NIR lines.

* E-mail: gd232@cam.ac.uk

¹ <https://www.preds-ci.com/portal/home.php>

The Fe XIII NIR lines are commonly used to measure the electron density, although direct measurements cannot be provided: as their intensities are affected by both collisions with free electrons and protons and photo-excitation (PE) from the disk radiation, a prior knowledge of the density ALOS is needed (cf. the appendix in Del Zanna et al. 2023). In conjunction with measurements of EUV lines from the same ion, they provide the opportunity to estimate the density distribution along the line of sight, and assess if non-Maxwellian electron distributions are present (Dudík et al. 2014; Dudík et al. 2021).

One long-standing problem in solar physics has been the estimate of the local magnetic field. With some assumptions on the Alfvén waves in the corona, the Fe XIII NIR lines can be used to infer the coronal magnetic field, as described in Yang et al. (2020). However, a more direct way to obtain information on the coronal magnetic field is with spectropolarimetry.

As in the case of the electron density, a direct inversion of observables to obtain the magnetic field is not reliable due to the contribution ALOS in the observed signal. Therefore, it is necessary to synthesize the Stokes parameters using forward modelling and compare them with observations to validate the results and extract information about the magnetic field. Recently, DKIST CryoNIRSP has obtained unprecedented Stokes profiles of the stronger 10747 Å line (Schad et al. 2024). The forward modelling tool `pyCLE`, developed by Schad & Dima (2020), was then used to calculate the Stokes V signal using as input an MHD model. The resulting V signal was not close to the observed one. These studies led them to conclude that the longitudinal coronal magnetic field strengths at greater heights above the solar limb may be higher than those predicted by conventional global coronal models. They attribute this difference to limitations in their study, including the relatively low resolution of the employed model and the simplified treatment of the lower boundary conditions.

It has long been known that the populations of the ground configuration, producing the NIR lines, are strongly affected by PE and proton collisions; also, both level and magnetic sublevel populations are affected by cascading from higher levels, populated by electron collisions (see, e.g. House 1977; Sahal-Brechot 1977; Judge et al. 2006). Cascading is particularly important as it increases significantly the populations and as via collisional coupling destroys the polarization in the forbidden lines. In order to account for the cascading effects from the higher states to the ground configuration we need to consider large multi-level atomic models.

This makes the calculations of the intensities (and all the other Stokes profiles) for 3-D forward models extremely time-consuming and it is therefore important to reduce the atomic models. An approach was developed by Judge et al. (2006) and used within the “Coronal Line Emission” (CLE) FORTRAN programs, which have been integrated in the SolarSoft FORWARD IDL package (Gibson et al. 2016). The starting point was older and incomplete atomic rates for an ion model comprising of 27 states. Such model was reduced to a 3-state model, and ad-hoc corrections were included to take into account the effects of cascading from the higher states (by increasing the collisional rates), and of the associated depolarization (with an ad-hoc parameter), by comparing the results of the 3-state with those from the 27-state model.

The need to consider improved atomic rates and a model larger than the 27-states one to account of the cascading effects was pointed out by one of us (GDZ) during the first DKIST coronal workshop at Maui to T. Schad; a Python version of CLE (`pyCLE`) was developed and used by Schad & Dima (2020) to show how the predicted intensities of the NIR lines change by reducing the CHI-

ANTI version 8 (Del Zanna et al. 2015) 749 states model to the lowest 27 and 100 states. They noted that the largest model adopted by Judge et al. (2006) also had 27 states, and showed that differences in the line intensities of the order of 10% can occur, when compared to the 749-state model. They concluded that at least 100 atomic states were needed in order to obtain accurate results while undertaking SP computations.

We note that the magnetic field information in the Fe XIII forbidden lines is contained in the Stokes parameter ratios U/Q and V/I' ($I' = dI/d\lambda$). These lines, being in the saturated Hanle regime for coronal magnetic field strengths, are sensitive only to the magnetic field orientation through Hanle effect, determined using the ratio U/Q , and not to the magnetic field strength. The line-of-sight component of the magnetic field strength can be derived from V/I' . Given this, if one considers the Stokes parameter ratios V/I' and U/Q , the effects of the cascades from higher states appear to cancel out, considering their expressions (Casini & Judge 1999). However, we demonstrate in the Appendix that this cancellation occurs primarily for large atomic models. For smaller atomic states, the cascading effects in the ratios do not cancel out. Moreover, obtaining these ratios requires calculating the full Stokes profiles (I , Q , U , V) by solving a multi-level atomic system for the density matrix elements and integrating ALOS to enable meaningful comparison with observations, a process that benefits from the use of reduced atomic models. Also, calculating V/I' produces additional noise to already very noisy data, and it is probably one of the reasons why the previous studies by Lin et al. (2004); Schad et al. (2024) considered all the Stokes profiles to estimate the magnetic field.

Recently, P-CORONA, a general suite of codes to perform forward modelling and predict the SP signal in allowed and forbidden lines was developed by one of us (SD), see Supriya et al. (2021), as part of the POLMAG EU-funded project². The above three suites of SP codes are all based on the density matrix formalism and various approximations described by Landi Degl’Innocenti & Landolfi (2004), although some differences are present.

Our ultimate goal is to improve the atomic modelling for Fe XIII, but also benchmark the various codes. This is carried out within an ISSI team³. Such comparisons are important. For example, whilst developing `pyCLE`, Schad & Dima (2020) found a significant bug in the CLE FORTRAN code which was subsequently fixed.

In this paper, we provide some example reduced models, and show how spectral line intensities and Stokes parameters differ from those obtained with the full model, for a range of cases. The methods we propose are general and we plan to extend them to other spectral lines in a future paper.

2 METHODS

The largest-scale scattering calculations for Fe XIII were carried out by Del Zanna & Storey (2012) as part of a long-term programme to improve the atomic data for the soft X-rays. The main calculations adopted the R -matrix suite of codes and included a complete set of the main $n = 4$ configurations, producing 749 fine-structure states. Significant resonance enhancement for some $n = 4$ configurations was found.

A distorted-wave calculation which included the main $n =$

² <http://research.iac.es/proyecto/polmag>

³ <https://teams.issibern.ch/middlecorona/>

5, 6 configurations, giving rise to 3066 fine-structure levels was also carried out, finding that cascading from the $n = 5, 6$ states affected the lower level populations by less than 10%. Given the limitations of the CHIANTI model atoms at the time, only the model with the 749 states was included in version 8 (Del Zanna et al. 2015), and is still the same in the latest version 11 (Dufresne et al. 2024).

The obvious question arises: what is the uncertainty in the large atomic models, to be used as a guide to how close the reduced models should be? The answer is not simple. One of us (GDZ) developed a simple method whereby different atomic calculations (of similar accuracy in principle) are compared, and from the scatter of the values an uncertainty for each single rate is obtained. These uncertainties are then propagated with a Monte Carlo method, by varying the rates randomly. The scatter in the resulting emissivities in a single spectral line is a measure (more of an upper limit) of the uncertainty. Such method was applied to the EUV lines of Fe XIII (Yu et al. 2018) and to the NIR lines (Yang et al. 2020). The estimated uncertainty in the NIR ratio is about 5% at a density of 10^8 cm^{-3} .

Considering also that it would be difficult to obtain measurements of Stokes parameters any better than 5%, we think that for most applications a reduced model which gives results to within about 5% those of the full model is a reasonable choice.

The main physical processes to consider in these computations are collisional excitation and de-excitation processes due to electrons, protons, and PE of the disk radiation. It has long been known that proton rates affect the populations of the ground configuration of coronal ions. We use here the CHIANTI proton rates which are J -resolved. The same rates are used by PyCLe and P-CORONA, although we note that the M -resolved rates should be used instead. The issue of calculating M -resolved proton rates for coronal ions is a complex one and will be addressed in a future paper.

PE from the disk is simple to include: as the radiation is effectively a continuum, it is well approximated with a black-body of 6100 K at the wavelengths of the Fe XIII NIR lines. The PE rate when the radiation is a continuum has traditionally been included in the literature as a modification of the A-value. The CHIANTI codes follow that approach by first constructing a matrix of photoexcitation rates and one for the corresponding stimulated emission rates (which are normally negligible). These matrices are then added to the matrix of the A-values before solving for the level populations. As already mentioned, PE is a strong effect, so it is impossible to infer the electron density (average ALOS) without knowing a priori its distribution. Hence, forward modelling needs to be carried out. The same reasoning applies to the Stokes parameters: one needs to calculate them for each point in a coronal volume, then perform integrations ALOS. This is easily carried out by P-CORONA, but the computing times for large models are very long, as we point out below with some examples.

2.1 Selecting key states

The method of finding a reduced model is very simple. We calculate the populations of the ground configuration states for a range of parameters, including proton rates and PE, then trace which higher states contribute via cascading, and include in the model only those above some threshold (a fraction of a percent). For example, if we consider the 10798 Å line we need to study in detail the population of the upper state, the $3s^2 3p^2 \ ^3P_2$. At $1.1 R_\odot$, $\log \text{Ne}=8$, and with a 6100 K black-body the population of this state is by 67% due to cascading.

The largest contributor to cascading (14%) comes from level

Table 1. Selected 55 states for Fe XIII.

Lev.	Conf.	LSJ	E_{exp}	E_t
1	$3s^2 3p^2$	3P_0	0.000	0.000
2	$3s^2 3p^2$	3P_1	0.085	0.081
3	$3s^2 3p^2$	3P_2	0.169	0.167
4	$3s^2 3p^2$	1D_2	0.438	0.451
5	$3s^2 3p^2$	1S_0	0.834	0.858
6	$3s 3p^3$	5S_2	1.956	1.911
7	$3s 3p^3$	3D_1	2.617	2.608
8	$3s 3p^3$	3D_2	2.619	2.610
9	$3s 3p^3$	3D_3	2.644	2.635
10	$3s 3p^3$	3P_0	2.997	3.001
11	$3s 3p^3$	3P_1	3.004	3.008
12	$3s 3p^3$	3P_2	3.010	3.013
13	$3s 3p^3$	1D_2	3.302	3.320
14	$3s 3p^3$	3S_1	3.786	3.839
15	$3s^2 3p 3d$	3F_2	3.920	3.968
16	$3s^2 3p 3d$	3F_3	3.981	4.031
17	$3s 3p^3$	1P_1	3.992	4.049
18	$3s^2 3p 3d$	3F_4	4.073	4.121
19	$3s^2 3p 3d$	3P_2	4.432	4.507
20	$3s^2 3p 3d$	3P_1	4.510	4.580
21	$3s^2 3p 3d$	1D_2	4.546	4.619
22	$3s^2 3p 3d$	3P_0	4.570	4.632
23	$3s^2 3p 3d$	3D_1	4.616	4.687
24	$3s^2 3p 3d$	3D_2	4.641	4.715
25	$3s^2 3p 3d$	3D_3	4.640	4.719
26	$3s^2 3p 3d$	1F_3	5.075	5.180
27	$3s^2 3p 3d$	1P_1	5.201	5.305
28	$3p^4$	3P_2	5.389	5.492
31	$3p^4$	1D_2	-	5.715
33	$3s 3p^2 3d$	5F_2	-	5.797
34	$3s 3p^2 3d$	5F_3	-	5.829
35	$3s 3p^2 3d$	5F_4	-	5.875
42	$3s 3p^2 3d$	3F_2	6.102	6.217
45	$3s 3p^2 3d$	5P_3	-	6.430
49	$3s 3p^2 3d$	3P_2	-	6.608
52	$3s 3p^2 3d$	3G_3	-	6.908
56	$3s 3p^2 3d$	3D_2	6.869	6.991
59	$3s 3p^2 3d$	1F_3	-	7.110
60	$3s 3p^2 3d$	3F_2	7.089	7.217
61	$3s 3p^2 3d$	3F_3	7.140	7.268
64	$3s 3p^2 3d$	1P_1	-	7.345
65	$3s 3p^2 3d$	3F_4	7.218	7.346
72	$3s 3p^2 3d$	3D_2	7.447	7.580
74	$3s 3p^2 3d$	3F_2	-	7.667
75	$3s 3p^2 3d$	3F_3	-	7.708
76	$3s 3p^2 3d$	3F_4	-	7.731
77	$3s 3p^2 3d$	1D_2	-	7.765
81	$3s 3p^2 3d$	1D_2	-	8.045
83	$3s 3p^2 3d$	1P_1	-	8.260
84	$3s 3p^2 3d$	3P_2	8.179	8.311
85	$3s 3p^2 3d$	3P_1	-	8.379
86	$3s 3p^2 3d$	3P_0	-	8.381
87	$3s 3p^2 3d$	1F_3	-	8.602
90	$3s^2 3d^2$	3F_4	-	8.867
91	$3s 3p^2 3d$	1D_2	-	8.897

E_{exp} are the experimental energies in Rydbergs. E_t are those obtained from the scattering target, see Del Zanna & Storey (2012). Lev. is the level number of the CHIANTI 749-states model.

14 ($3s\ 3p^3\ ^3S_1$), which is populated by cascading only by 3%, with level 84 ($3s\ 3p^2\ 3d\ ^3P_2$) being the main contributor, which we have included. 13% of the population comes from the next higher level 4 ($3s^2\ 3p^2\ ^1D_2$) within the ground configuration, which in turn is populated by 61% via cascading, mostly from many states of the $3s\ 3p^3$ and $3s^2\ 3p\ 3d$ configurations, which in turn are also populated partly by cascading which needs to be followed. The next state contributing is level 20 ($3s^2\ 3p\ 3d\ ^3P_1$) which produces the resonance transition, hence is almost entirely populated by excitation from the ground state. The next contribution, by 5%, is from level 9 ($3s\ 3p^3\ ^3D_3$), which in turn is populated for 15% by cascading from level 28 ($3p^4\ ^3P_2$). Another 5% comes from level 25 ($3s^2\ 3p\ 3d\ ^3D_3$) which has a small cascading contribution (9%) with over 3% from states 84 and 90, which we have included in the model. Levels 11, 16, 23, and 24 each contribute about 3%, so they need to be included as well as any higher states with significant cascading contributions to those levels. Finally, about 5% comes from the 6,15, and 19 levels.

The same procedure was applied to the $3s^2\ 3p^2\ ^3P_1$. This is to make sure that all the main states contributing to its population by cascading effects are included.

It is clear that the number of higher states that need to be included initially grows considerably. However, contributions gradually decrease. Typically, higher states are populated by electron collisions from the ground configuration, with increasingly smaller cascading contributions for increased excitation energy.

It is therefore possible to select a reasonably small number of states which produce the main cascading and populations of the two main states within a few percent. There are clearly many choices depending on which accuracy is needed. We present a newly constructed model with a *selected* set of 55 states. This includes all the lowest 28 states and selected 27 states which are the major contributors to the populations of the two main states via cascading. For an accuracy of 5 percent (or better) we suggest this model of *selected* 55 J -resolved states, listed in Table 1 and provided in CHIANTI format. We used this model for line intensity calculations with the CHIANTI programs and the polarization signal with P-CORONA calculations. The model gives very good results for a range of coronal conditions, as shown below.

Clearly, the method can easily be applied to other physical conditions and automatized. The method focuses on the two NIR transitions. However, we have also checked that the model produces populations of the ground state close to those calculated with the full model, as shown in the Appendix. As almost all the population of the ion for coronal conditions is in the 3P states, these are the states populating the higher ones by electron collision. Therefore, the model also produces accurate populations for any higher state where cascading is negligible.

2.2 Merging states

The density matrix formalism and approximations described by Landi Degl'Innocenti & Landolfi (2004) requires J -resolved states. However, if one is interested in modelling just the intensities of the lines, a better approach is that of merging states, or super-levels. As in the previous case, there are many options. We have chosen to keep the lowest 27 states J -resolved, and added six super-levels (described in Table 2), for a total of 33 states. We also provide CHIANTI files to be used.

The current standard CHIANTI structure unfortunately only allows LSJ states. However, in principle each state could have any label, the only quantities used from the energy file for the calculations are the energies of the states (in inverse cm) and the mul-

Table 2. Merged states

Lev	CHIANTI Levs	Configuration	states merged
28	28–34	$3p^4$	$^3P, ^1D_2$
29	32–44	$3s\ 3p^2\ 3d$	$^5F, ^5D, ^3F$
30	45, 47–54	$3s\ 3p^2\ 3d$	$^5P, ^3P, ^3G$
31	55–64	$3s\ 3p^2\ 3d$	$^3D, ^1G_4, ^1F_3, ^3F, ^3D, ^1P_1$
32	65–77	$3s\ 3p^2\ 3d$	$^3F, ^3D, ^3P, ^3S_1, ^1D_2$
33	78–87,91	$3s\ 3p^2\ 3d$	$^3D, ^1D_2, ^1S_0, ^1P_1, ^3P, ^1F_3, ^1D_2$

Lev is the merged level number, Levs the original level numbers.

tiplicity, calculated as $g = 2J + 1$. When merging the k states we have summed the multiplicities to obtain the multiplicity of the merged state, then wrote in the file a corresponding fictitious J value. The energy E_m of the merged state is the weighted average: $E_m = (\sum_k g_k E_k) / \sum_k g_k$. From these averaged values we have recalculated averaged wavelengths for the transitions to the lower states.

We have then calculated the excitation rate coefficients from each of the lower 27 states to each of the merged states. CHIANTI uses a Burgess & Tully (1992) scaled value of the adimensional normalised rate coefficient called the effective collision strength Υ , calculated from the cross-section by assuming a Maxwellian electron distribution. We have first obtained 18 Υ_{ij} values over a very large temperature range, from 10^4 to 10^8 K, with steps of 0.2 dex around the peak formation temperature, then obtained the $\Upsilon_{im} = \sum_k \Upsilon_{ik}$. After that we have scaled the Υ_{im} and extrapolated the values to obtain the limit points, to produce the CHIANTI-format rates. When merging transitions of different Burgess & Tully (1992) type, we have chosen to adopt type 2 (forbidden transition), and in any case visually inspected each scaled rate. We note that the choice of type of transition for the scaling is essentially irrelevant. It is just a transformation so the interpolation is performed on more smoothly-varying rates. As long as there are sufficient grid points. The extrapolation to the limit points is also irrelevant, given the large temperature range the data are provided. There is no need to consider the excitation rates among the merged states as they are essentially populated from the ground configuration states.

Regarding the A-values, we have kept those among the lowest 27 states. The last step was to calculate the A-values A_{im} between the J -resolved 27 states i and the merged states m . In order to satisfy Einstein's relations between the radiative coefficients, they are: $A_{im} = (\sum_k g_k A_{ik}) / \sum_k g_k$. We have neglected radiative transitions among the merged states as all the main decays from the higher states are to the lower 27 states, even though in principle they could be added with the appropriate averaging.

3 RESULTS

3.1 Validation of the reduced atomic models

We initially follow Schad & Dima (2020), by plotting the ratio of the local emissivities in the two NIR lines obtained with a range of models, relative to the current 749-state CHIANTI model. The emissivities have been calculated with the CHIANTI IDL programs. As in Schad & Dima (2020) we have selected the lowest 27 and 100 states. In addition, we show in Figure 1 the results of

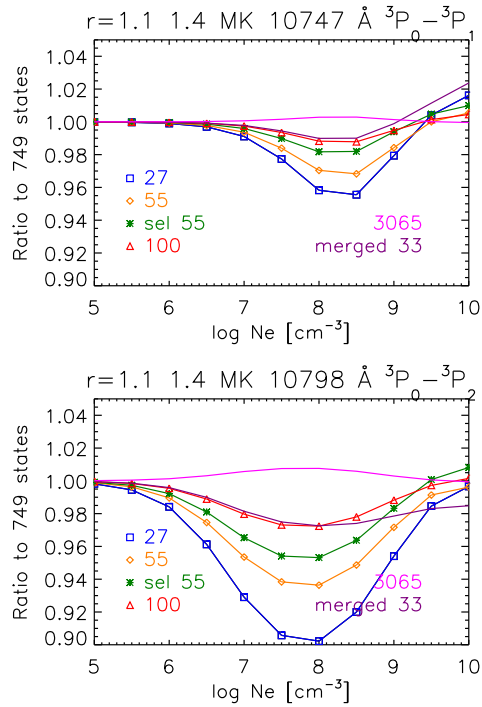


Figure 1. The two plots show the ratio of the local emissivities in the two NIR lines obtained with 27, 91, and 200 states, relative to the values obtained with the current 749-state CHIANTI model. They also show the selected 55 states and the merged 31 states. The emissivities were calculated at a distance of $1.1 R_{\odot}$, at 1.4 MK, PE with a 6100 K black-body, and as a function of electron density.

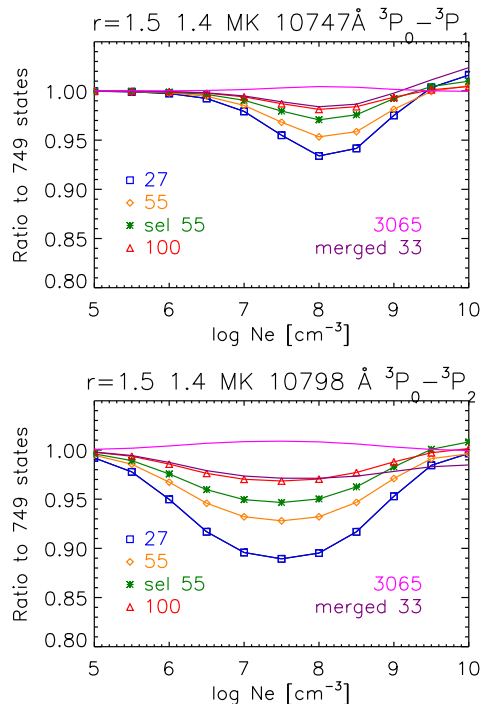


Figure 2. The same as Figure 1, calculated at a distance of $1.5 R_{\odot}$ at 1.4 MK.

Table 3. Relative populations for the states in the $3s^2 3p^2$ ground configuration of Fe XIII.

Model	3P_0 10^{-1}	3P_1 10^{-1}	3P_2 10^{-2}	1D_2 10^{-3}	1S_0 10^{-5}
3065 states	7.59	1.57	8.19	1.90	3.41
749 states	7.60	1.57	8.13	1.88	3.37
749 (no PE)	8.36	0.89	7.36	1.71	3.43
100 states	7.64	1.55	7.91	1.79	3.26
55 states	7.70	1.52	7.61	1.67	3.20
sel. 55 states	7.67	1.54	7.75	1.74	3.25
merged 33	7.63	1.55	7.91	1.81	3.29
27 states	7.75	1.54	7.73	1.58	3.19
sel. 55 states (P-CORONA)	7.67	1.54	7.74	1.73	3.25

The models are at a distance of $1.1 R_{\odot}$, at 1.4 MK, PE with a 6100 K black-body, and $N_e = 10^8 \text{ cm}^{-3}$.

Table 4. Alignment for the states within the $3s^2 3p^2$ ground configuration of Fe XIII, obtained from P-CORONA and different atomic states

Model	3P_1 10^{-2}	3P_2 10^{-2}	1D_2 10^{-3}
27 states	9.29	1.89	-1.51
55 states	9.07	1.80	-1.47
sel. 55 states	8.91	1.77	-1.43
100 states	8.77	1.72	-1.38
200 states	8.74	1.71	-1.37
749 states	8.58	1.66	-1.30

The models are at a distance of $1.1 R_{\odot}$, at 1.4 MK, PE with a 6100 K black-body, and $N_e = 10^8 \text{ cm}^{-3}$.

the selected 55 states, as well as those of just selecting the lowest 55 states. Finally, we also show the ratios obtained with the more complete 3065 state model and with the reduced merged 33 state model. Figure 1 shows the results calculated for a distance of $1.1 R_{\odot}$ and an electron temperature of 1.4 MK, typical of the quiet Sun (see, e.g. Gibson et al. 1999). The results for the 27 and 100-states models appear to be the same as those obtained by Schad & Dima (2020), as expected since they used the same atomic data. Note that at such distance the electron density is typically 10^8 cm^{-3} . For the stronger line (measured by Lyot at 10746.80 \AA in air), all models are within 2%, except the 27-state model, where there is a discrepancy of about 5%. For the weaker line (measured by Lyot at 10797.95 \AA in air), the 27-state model under-predicts the emissivity by about 10%, while the selected 55-state model is within 5%. The reduced merged 33-state model performs extremely well, producing results close to the larger 100-state model, i.e. within about 2% the 749-state model.

The relative populations of the ground state are all reassuringly close to those obtained with the 749-state model, with the exception of the 27-state model case, as shown in the Appendix.

A similar picture is present at a distance of $1.5 R_{\odot}$, as shown in Figure 2. Note that in the quiet Sun at such distances one expects a density less than 10^7 cm^{-3} , and as before the selected 55-state model is within 5% for the weaker line. Similar plots at a slightly

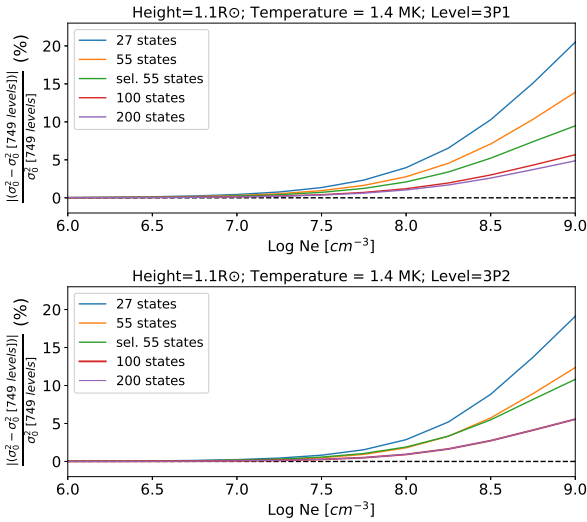


Figure 3. The two panels show the percentage variation of the upper level alignment (σ_0^2) obtained with 27, 55 (both from CHIANTI 10 and reduced model), 100 and 200 states, relative to the values obtained with the 749 states for the Fe XIII 10746.8 Å line. These computations were done for a distance of 1.1 R_\odot , at 1.4 MK, PE with a 6100 K black-body, and as a function of electron density.

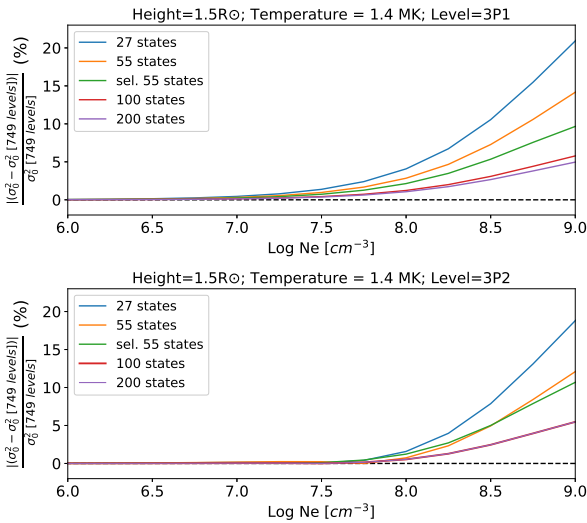


Figure 4. The same as Figure 3 but at a distance of 1.5 R_\odot .

higher temperature of 1.8 MK adopted by Schad & Dima (2020) are shown in the Appendix in Figure A2. The results are very similar. When an active region is present, the ion emission is a superposition of the large-scale quiet Sun corona and a diffuse higher-temperature of about 2 MK. Therefore, we expect the accuracy of the models to be similar also when modelling an active region.

Table 3 shows the relative populations for the main states in the $3s^2 3p^2$ ground configuration of Fe XIII, for a distance of 1.1 R_\odot , at 1.4 MK, PE with a 6100 K black-body, and at an electron density of 10^8 cm^{-3} . It is reassuring to see that the larger 3065 states model produces virtually the same populations as the CHIANTI 749 states model, except the 3P_2 state, where the larger model produces a population 0.7% larger due to extra cascading.

The third row in Table 3 shows the populations obtained with

out including PE, to confirm the large effect it has even in the low corona. The following rows indicate the relative populations for the other models. The last row shows the values obtained from P-CORONA using the selected 55 states, to confirm that the CHIANTI and P-CORONA codes produce consistent results.

Following this, using P-CORONA⁴, we compute the relative differences in the atomic alignment (σ_0^2) of the 3P_1 and 3P_2 levels in Figures 3 and 4. Atomic alignment quantifies the contribution to the linear polarization due to scattering with $\sigma_0^2(J) = \frac{\rho_0^2(J)}{\rho_0^0(J)}$, where ρ_0^K 's are the multipolar components of the atomic density matrix (see Landi Degl'Innocenti & Landolfi 2004). Thus the atomic level alignment of the 3P_1 and 3P_2 states contributes to the scattered polarization signal of the lines at 10747 Å and 10798 Å respectively. The relative difference in σ_0^2 is computed with respect to the 749 levels for the cases of 27, 55, selected 55, 100 and 200 states.

The plasma conditions in Figures 3 and 4 are the same as in Figures 1 and 2 respectively. The relative difference in the atomic alignment in both the levels is below 5% for coronal densities of 10^8 cm^{-3} or below. The relative differences in atomic alignment increase as we consider higher densities. However, the overall atomic alignment remains low in these cases, as increased collisions tend to destroy the atomic alignment. Therefore, the large relative differences are a result of the small values involved. For a better comparison, we refer readers to Figure 4 in Schad & Dima (2020), where the actual alignment values for the upper level of the relevant lines are plotted.

Table 4 shows the alignment for the states within the $3s^2 3p^2$ ground configuration of Fe XIII, obtained from P-CORONA and various reduced atomic models. It is clear that the alignment is not much sensitive to the atomic models for the representative plasma parameters considered.

3.2 Computing times

To show the importance of having a reduced atomic model when performing SP large-scale calculations, we have run P-CORONA for a single point in the corona, with typical parameters. The computing time, obtained with a single core, is shown in the second column of Table 5. For a realistic 3D forward model, we have then scaled these times according to typical small volumes, e.g. a 257x512x643 MURaM simulation and the volume corresponding to a typical DKIST CryoNISR single-pointing slit scan, at 1'' resolution. In coronal mode, the 4'' slit can be scanned by about 3'', so we have considered a box of 240x240x240.

P-CORONA is parallelized (MPI+OpenMP), but even with a large number of cores it is clear that reduced atomic models are really necessary. The computing time required in 100 states is 3.6 times larger than that of 55 states. The reduction in computational time achieved with the selected 55-state model, while maintaining accuracy, is a significant advantage in addressing the complex problem of coronal line inversions. This efficiency allows for more feasible and timely analysis of coronal observations, particularly in large-scale SP studies.

3.3 Spectral synthesis with a realistic MHD model

In this section, we show the results of the forward synthesis of the frequency-integrated intensity and polarization signals using 3D

⁴ <https://polmag.gitlab.io/P-CORONA/index.html>

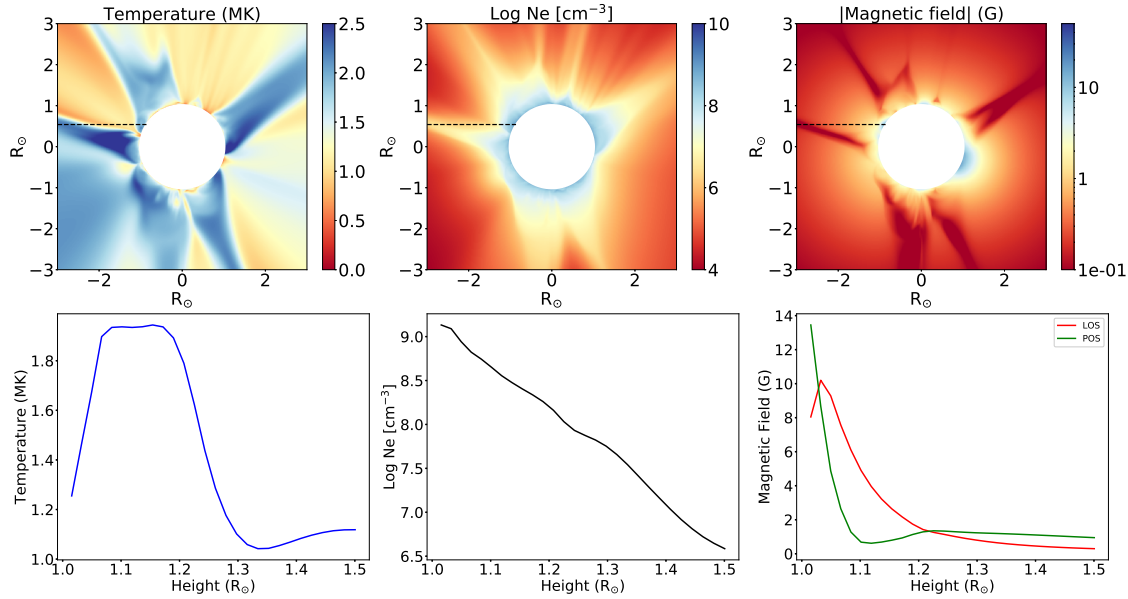


Figure 5. The top panels show the temperature, electron number density, and magnetic field strength for the PSI Eclipse 2024 model in the plane of the sky (POS). The dashed line indicates the direction along which we consider the variation of these quantities, as shown in the bottom panel, used later in Figures 6 and 7. The third column in the bottom panel shows the plane-of-sky (POS) and line-of-sight (LOS) components of the magnetic field in the selected direction.

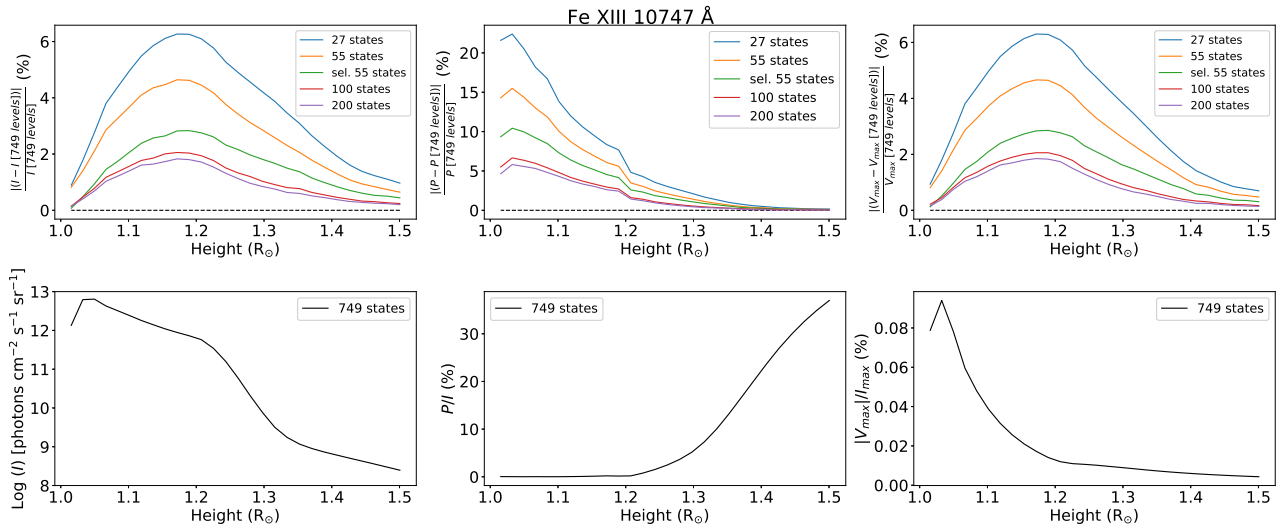


Figure 6. The frequency integrated intensity, I , (in the first column) and polarization signals (the total linear polarization P in the second column and the maximum of circular polarization V_{max} in the last column) of the Fe XIII 10747 Å line. The spectro-polarimetric signals are computed in the PSI eclipse 2024 model along the dashed line indicated in Figure 5. The top panel shows the relative difference in the spectral signals and the bottom panel, the variation of them with height computed for the 749 states.

coronal MHD models by PSI. Our aim is to compute the differences in these signals in a realistic 3D MHD model while considering reduced atomic models. We took the recent PSI model corresponding to the total solar eclipse on 8 April, 2024⁵. This was constructed using a time-dependent MHD model that was updated in near real-time with the latest measurements of the photospheric magnetic field (Mikić et al. 2018; Boe et al. 2021, 2022; Lionello et al. 2023). We use a time snapshot of this model, described in Downs et al. (2024). The basic plasma parameters re-

quired for our computations, temperature, electron number density, and magnetic fields, are shown in Figure 5. We consider a 1D cut (indicated as dashed lines) in the plane of the sky (POS) and show in the bottom panels of Figure 5 the variations of these parameters with height. In the bottom right panel of this Figure, we show both the POS and LOS magnetic fields in the chosen direction. We have chosen such 1D cut for our representative computations with P-CORONA, as a full 3D one would take too long when considering the larger-scale models.

We restrict our computations till $1.5 R_{\odot}$, beyond which the density drops below 10^7 cm^{-3} and there would be very little signal

⁵ <https://www.predsci.com/eclipse2024>

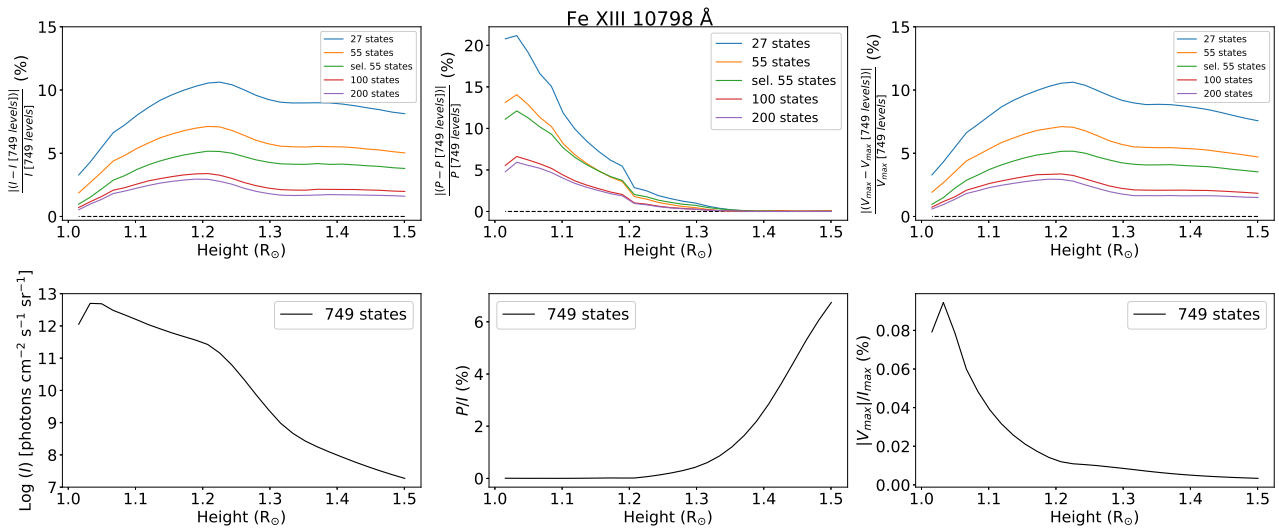


Figure 7. Same as Figure 6 but for the Fe XIII 10798 Å line.

Table 5. An estimate of the total computing time required for full forward modelling using P-CORONA when different number of atomic levels are considered.

No. of levels	Single point	MURaM model (257x512x643)	1'' resolution (240x240x240)
27 states	2.3s	54055 hrs	8832 hrs
55 states	7.4s	173917 hrs	28416 hrs
100 states	26.9s	632213 hrs	103296 hrs
749 states	438m	12691276 hrs	2073600 hrs

For comparison, the computing times are calculated using a single core. P-CORONA is parallelized (MPI+OpenMP), so these numbers scale depending on the machine's efficiency and number of cores.

(also, DKIST CryoNIRSP can at most observe such distance). Our theoretical studies in the previous section show that the differences in the population and alignment of the concerned atomic levels does not change significantly with the number of atomic states used for these lower densities. We also find similar results, as shown in Figure 6 and Figure 7 for the Fe XIII 10747 Å and 10798 Å lines.

The bottom panels of these figures show the frequency integrated radiances I , the percentage of total linear polarization $P = \sqrt{Q^2 + U^2}$ relative to I , and the percentage of maximum circular polarization V_{max} relative to I_{max} . These values are calculated by integrating ALOS from $-0.02 R_{\odot}$ to $+0.02 R_{\odot}$, approximating the plane-of-sky values. The upper panels in Figures 6 and 7 show the percentage differences between the results obtained with the various reduced models and the larger-scale 749-state model. The 55-state *selected* model performs very well, with less than 2% differences. The relative difference in the total linear polarization is high close to the limb where the P/I is too low to be easily measured. Figure A5 shows the relative differences in the Stokes values presented in the top panel of the Figures 6 and 7, but for the ratios U/Q and $|V_{max}|/I_{max}$. The contribution from the higher levels through collisions and cascading almost cancel out in these ratios

while considering the 27-state model or larger. However, this is not true for smaller atomic models as shown in Figure A5.

4 CONCLUSIONS

We have provided as examples two reduced atomic models for use in large-scale computations of the intensities or the Stokes parameters of the Fe XIII NIR lines. These models provide significant savings in computing times. Obviously, an alternative way if one is interested in just the intensities would be to pre-calculate a lookup table, i.e. emissivities over a large parameter space in density, temperature and distance from the Sun, and then interpolate. We have shown with a range of calculations that line intensities and polarization signatures are still accurate to within 5%, which is comparable to the current uncertainties in the large-scale atomic model.

We demonstrated that the 55-state *selected* model performs well across a range of coronal conditions, preserving the essential physics of atomic transitions without the need for larger, more computationally demanding models. We also highlighted the efficiency of merging atomic states, which is especially useful for intensity calculations. While this method currently has limitations for polarization calculations, it still represents a highly accurate and computationally efficient approach. Other reduced models can be provided upon request.

The complexities of the optically thin solar corona are such that a better understanding of its physical state can only be achieved with routine large-scale forward models, to be compared to observations. One long-standing problem in solar physics has been the estimate of the local magnetic field. Recently, DKIST has shown that it is indeed capable of measuring the Stokes V, producing unprecedented polarized spectra of the 10747 Å line (Schad et al. 2024). A combination of the unprecedented DKIST CryoNIRSP observations with large-scale computations with P-CORONA using reduced atomic models will finally provide the much needed information. Though the Stokes ratios U/Q and V/I' , which contain the magnetic field information, are not significantly sensitive to cascading effects while considering large atomic models, the forward modelling computations required to calculate the individual Stokes parameters (I, Q, U, V) necessitate the use of reduced atomic mod-

els. Additionally, the forward modelling process, which forms the basis of inversion codes, can benefit from faster computations enabled by these reduced models.

Moving forward, the methodology used in developing reduced atomic models here will be extended to other spectral lines and ions, allowing their application in a wider range of coronal studies. This capability will be essential for future large-scale spectropolarimetric surveys, where computational efficiency is crucial for analyzing the vast amounts of data that will be collected and also in designing inversion methods.

In summary, the reduced atomic models presented in this paper provide a practical and efficient solution for spectropolarimetric modelling in the solar corona, offering a balance between computational speed and accuracy.

ACKNOWLEDGMENTS

We are grateful to Cooper Downs (Predictive Science Inc.) for providing the PSI simulation. GDZ acknowledges support from STFC (UK) via the consolidated grant to the atomic astrophysics group at DAMTP, University of Cambridge (ST/T000481/1). This research was supported by the International Space Science Institute (ISSI) in Bern, through the ISSI International Team project # 23-572 on *Models and Observations of the Middle Corona*, led by GDZ. HDS acknowledges support from the Agencia Estatal de Investigación del Ministerio de Ciencia, Innovación y Universidades (MCIU/AEI) under the grant “Polarimetric Inference of Magnetic Fields” and the European Regional Development Fund (ERDF) with reference PID2022-136563NB-I00/10.13039/501100011033. HDS thanks Ángel de Vicente (IAC) for useful discussions. Finally, we thank the reviewers for useful comments.

DATA AVAILABILITY

The CHIANTI-format models developed for this paper and the equivalent one in P-CORONA format are available on ZENODO at <https://doi.org/10.5281/zenodo.1398811>

Further data and programs will be posted in CHIANTI-VIP⁶, a portal for advanced atomic data and models.

REFERENCES

- Boe B., Habbal S., Downs C., Druckmüller M., 2021, *ApJ*, 912, 44
- Boe B., Habbal S., Downs C., Druckmüller M., 2022, *ApJ*, 935, 173
- Burgess A., Tully J. A., 1992, *A&A*, 254, 436
- Casini R., Judge P. G., 1999, *ApJ*, 522, 524
- Del Zanna G., DeLuca E. E., 2018, *ApJ*, 852, 52
- Del Zanna G., Dere K. P., Young P. R., Landi E., Mason H. E., 2015, *A&A*, 582, A56
- Del Zanna G., Samra J., Monaghan A., Madsen C., Bryans P., DeLuca E., Mason H., Berkeley B., de Wijn A., Rivera Y. J., 2023, *ApJS*, 265, 11
- Del Zanna G., Storey P. J., 2012, *A&A*, 543, A144
- Del Zanna G., Storey P. J., 2022, *MNRAS*, 513, 1198
- Del Zanna G., Storey P. J., Badnell N. R., Andretta V., 2020, *ApJ*, 898, 72
- Downs C., Linker J. A., Caplan R. M., Mason E. I., Riley P., Davidsson R., Reyes A., Palmerio E., Lionello R., Turtle J., Ben-Nun M., Stulajter M. M., Titov V. S., Torok T., Upton L. A., Attie R., Jha B. K., Arge C. N., Henney C. J., Valori G., Strecker H., Calchetti D., Germerott D., Hirzberger J., Suarez D. O., Rodriguez J. B., Solanki S. K., Cheng X., Wu S., 2024, *Science*, submitted
- Dudík J., Del Zanna G., Mason H. E., Dzifčáková E., 2014, *A&A*, 570, A124
- Dudík J., Del Zanna G., Rybák J., Lörinčík J., Dzifčáková E., Mason H. E., Tomczyk S., Galloy M., 2021, *ApJ*, 906, 118
- Dufresne R. P., Del Zanna G., Young P. R., Dere K. P., Deliporanidou E., Barnes W. T., Landi E., 2024, *arXiv e-prints*, p. arXiv:2403.16922
- Fehlmann A., Giebink C., Kuhn J. R., Messersmith E. J., Mickey D. L., Scholl I. F., James D., Hnat K., Schickling G., Schickling R., 2016, in *Ground-based and Airborne Instrumentation for Astronomy VI* Vol. 9908 of *Proc. SPIE*, Cryogenic near infrared spectropolarimeter for the Daniel K. Inouye Solar Telescope. p. 99084D
- Gibson S., Kucera T., White S., Dove J., Fan Y., Forland B., Rachmeler L., Downs C., Reeves K., 2016, *Frontiers in Astronomy and Space Sciences*, 3, 8
- Gibson S. E., Fludra A., Bagenal F., Biesecker D., del Zanna G., Bromage B., 1999, *J. Geophys. Res.*, 104, 9691
- House L. L., 1977, *ApJ*, 214, 632
- Judge P. G., 1998, *ApJ*, 500, 1009
- Judge P. G., Habbal S., Landi E., 2013, *Sol. Phys.*, 288, 467
- Judge P. G., Low B. C., Casini R., 2006, *ApJ*, 651, 1229
- Landi E., Habbal S. R., Tomczyk S., 2016, *Journal of Geophysical Research (Space Physics)*, 121, 8237
- Landi Degl’Innocenti E., Landolfi M., 2004, *Polarization in Spectral Lines*. Vol. 307
- Lin H., Kuhn J. R., Coulter R., 2004, *ApJ*, 613, L177
- Lionello R., Downs C., Mason E. I., Linker J. A., Caplan R. M., Ryot P., Titov V. S., DeRosa M. L., 2023, *ApJ*, 959, 77
- Lytot B., 1939, *MNRAS*, 99, 580
- Madsen C. A., Samra J. E., Del Zanna G., DeLuca E. E., 2019, *ApJ*, 880, 102
- Mikić Z., Downs C., Linker J. A., Caplan R. M., Mackay D. H., Upton L. A., Riley P., Lionello R., Török T., Titov V. S., Wijaya J., Druckmüller M., Pasachoff J. M., Carlos W., 2018, *Nature Astronomy*, 2, 913
- Penn M. J., 2014, *Living Reviews in Solar Physics*, 11, 2
- Rimmele T., McMullin J., Warner M., Craig S., Woeger F., Tritschler A., Cassini R., Kuhn J., Lin H., Schmidt W., Berukoff S., Reardon K., Goode P., Knoelker M., Rosner R., Mathioudakis M., DKIST TEAM 2015, *IAU General Assembly*, 22, 2255176
- Sahal-Brechot S., 1977, *ApJ*, 213, 887
- Samra J. E., Marquez V., Cheimets P., DeLuca E. E., Golub L., Hannigan J. W., Madsen C. A., Vira A., 2021, *arXiv e-prints*
- Samra J. E., Marquez V., Cheimets P., DeLuca E. E., Golub L., Hannigan J. W., Madsen C. A., Vira A., Adams A., 2022, *AJ*, 164, 39
- Schad T., Dima G., 2020, *Sol. Phys.*, 295, 98
- Schad T. A., Kuhn J. R., Fehlmann A., Scholl I. F., Harrington D., Rimmele T., Tritschler A., 2023, *ApJ*, 943, 59
- Schad T. A., Petrie G. J., Kuhn J. R., Fehlmann A., Rimmele T., Tritschler A., Woeger F., Scholl I., Williams R., Harrington D., Paraschiv A. R., Szente J., 2024, *Science Advances*, 10,

⁶ www.chianti-vip.com

eadq1604

Supriya H. D., Trujillo Bueno J., de Vicente Á., del Pino Alemán T., 2021, *ApJ*, 920, 140

Tomczyk S., Card G. L., Darnell T., Elmore D. F., Lull R., Nelson P. G., Streater K. V., Burkepille J., Casini R., Judge P. G., 2008, *Sol. Phys.*, 247, 411

Tomczyk S., Landi E., Burkepille J. T., Casini R., DeLuca E. E., Fan Y., Gibson S. E., Lin H., McIntosh S. W., Solomon S. C., Toma G., Wijn A. G., Zhang J., 2016, *Journal of Geophysical Research (Space Physics)*, 121, 7470

Yang Z., Bethge C., Tian H., Tomczyk S., Morton R., Del Zanna G., McIntosh S. W., Karak B. B., Gibson S., Samanta T., He J., Chen Y., Wang L., 2020, *Science*, 369, 694

Yu X., Del Zanna G., Stenning D. C., Cisewski-Kehe J., Kashyap V. L., Stein N., van Dyk D. A., Warren H. P., Weber M. A., 2018, *ApJ*, 866, 146

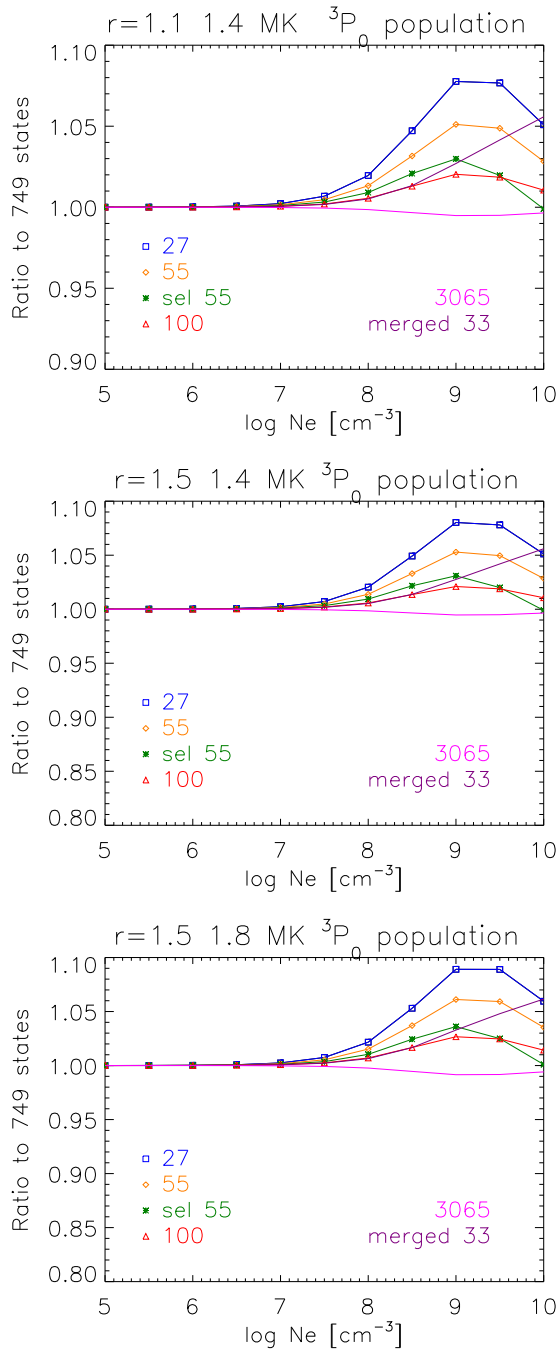


Figure A1. The populations of the ground state, relative to the values obtained with the 749-states model, for the temperatures and distances listed.

APPENDIX A: EXTRA MATERIAL

Figure A1 shows the populations of the ground state, relative to the values obtained with the 749-states model, for the two sets of parameters chosen for the main paper and for the case presented by Schad & Dima (2020), a distance of $1.5 R_{\odot}$ and a temperature of 1.8 MK. It is clear that differences are negligible, except in cases where the local density would be very high as in the core of an active region. In such a case the excited states become populated more and the differences reach a few percent.

Figure A2 shows the relative intensities of the two NIR lines, as in Figure 1, calculated at a distance of $1.5 R_{\odot}$ at 1.8 MK, for

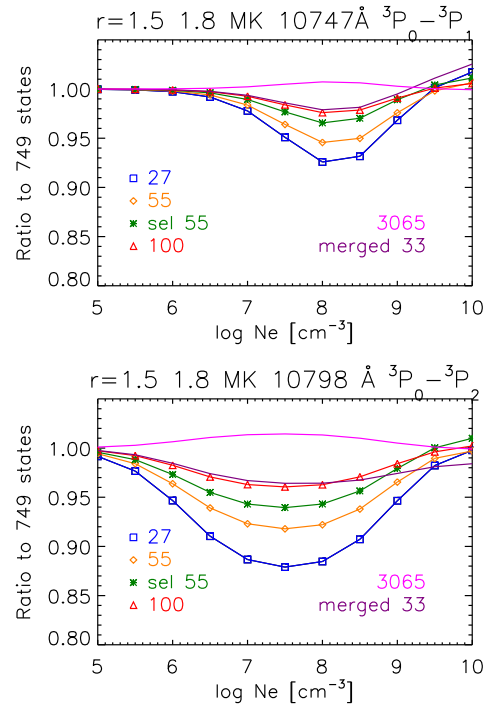


Figure A2. The same as Figure 1, calculated at a distance of $1.5 R_{\odot}$ at 1.8 MK.

comparison with the results shown by Schad & Dima (2020). Figures A3 and A4 show the variation of alignment for the above mentioned cases.

Figure A5 shows the relative differences in U/Q and $|V_{max}|/I_{max}$ for different atomic levels considered compared to the full 749 level calculations for both the Fe XIII lines. We compute the simpler frequency integrated $|V_{max}|/I_{max}$ as a proxy for V/I . These results are computed for the 1D variation in the PSI eclipse 2024 model shown in Figure 5. Along with the atomic models containing 27, 55, 100, and 200 states, we additionally compute the relative differences for models with 3, 10, and 20 states to highlight how the relative differences are significantly larger when cascading and collisional effects from higher states are not considered.

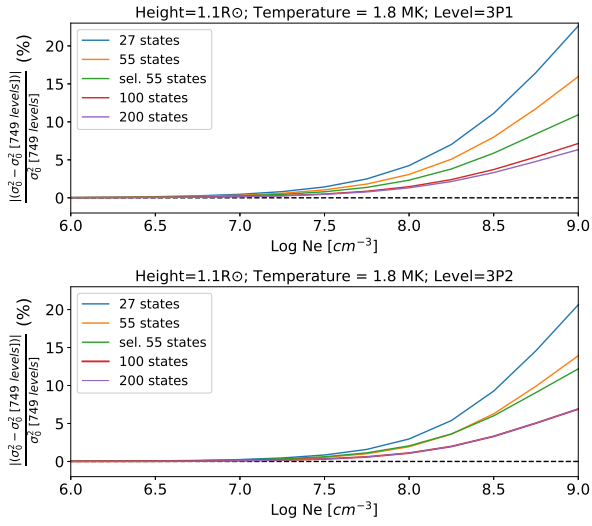


Figure A3. The same as Figure 3 but for a temperature of 1.8 MK.

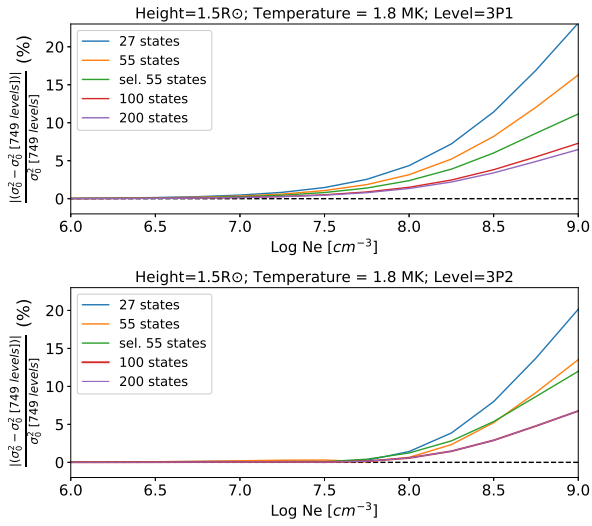


Figure A4. The same as Figure 4 but for a temperature of 1.8 MK.

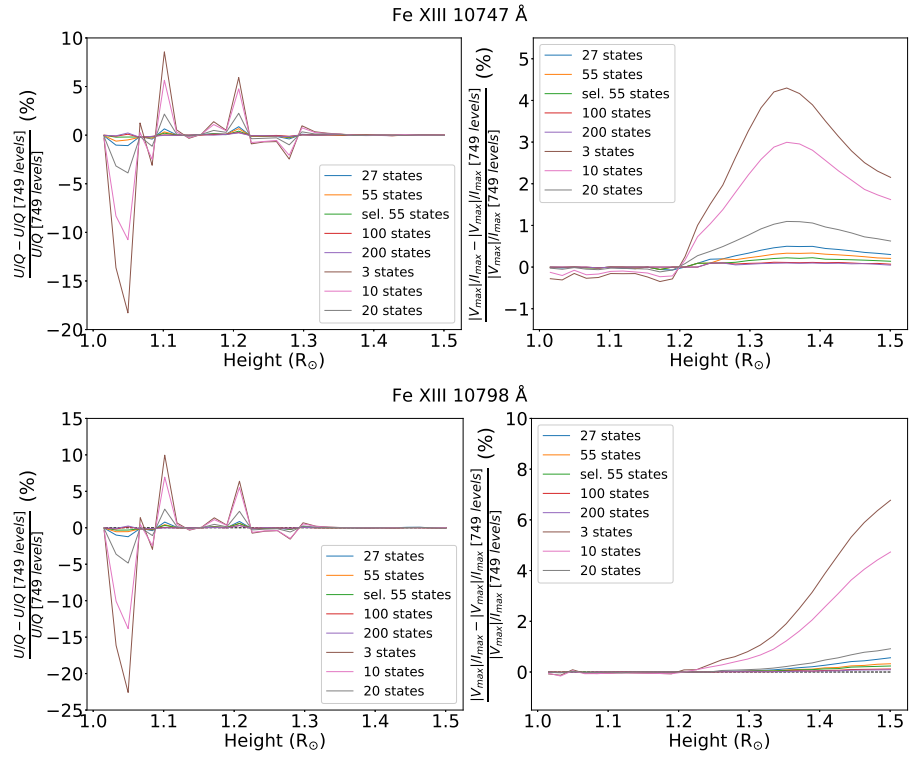


Figure A5. The left and right panels show the relative differences in the ratios U/Q and $|V_{max}|/I_{max}$, respectively, for 3, 10, 20, 27, 55, 100, and 200 states compared to the 749 levels computed in the PSI eclipse 2024 model, as shown in the bottom panel of Figure 5. The top and bottom panels correspond to the Fe XIII 10747 Å and 10798 Å lines, respectively.